Analysis and Comparison of Push–Pull Class-E Inverters With Magnetic Integration for Megahertz Wireless Power Transfer

Xiaosheng Huang, Yipeng Kong, Ziwei Ouyang, *Senior Member, IEEE*, Wei Chen, and Shuyi Lin

***Abstract*—This paper presents the circuit design and magnetic integration of push–pull class-E inverters for wireless power transfer (WPT) up to megahertz. The design criterion for achieving zero-voltage switching (ZVS) of a class-E inverter with coupled windings is derived mathematically. The approaches of magnetic integration for push–pull class-E inverters are analyzed and compared. Then, a new magnetic structure with hybrid magnetic materials is proposed to build the integrated inductors with either coupled windings or uncoupled windings. A 3-MHz WPT system is built to verify the analysis. The detailed comparison of the class-E inverters with magnetic integration is presented in terms of switch voltage, efficiency, harmonic currents, and thermal distribution. In the optimized design example, the switches keep ZVS over the entire load range without using any closed-loop control. The system efficiency reaches 87.1% at 350-W output power.**

***Index Terms*—Class-E, integrated magnetic, inverter, rectifier, wireless power transfer (WPT).**

NOMENCLATURE

v_S, v_{S1}, v_{S2}	Switch voltages.
ω	Angular frequency.
R	Equivalent load resistance of inverters.
i_R	Output current of the inverter.
I_R	Amplitude of i_R.
φ	Initial phase of i_R.
Q_L	$= \omega L_o/R$, loaded quality factor.
L_{in}	Inductance of windings L_{in1} and L_{in2}.
L_c	Mutual inductance of the coupled windings.
L_f	Leakage inductance of the coupled windings.
k_{in}	Coupling coefficient of the coupled windings.
$i_{\text{in1}}, i_{\text{in2}}$	Winding current.
I_{DC}	DC component, i.e., dc bias of i_{in1} and i_{in2}.
i_{Lf}	AC component of i_{in1} and i_{in2}.
C_f	Capacitance of C_{f1} and C_{f2}.
L_e	$= 2L_f$, equivalent resonant inductance for the coupled windings.
V_{in}	Input dc voltage.
q_e	$= 1/\omega\sqrt{L_e C_f}$, the normalized resonance frequency of L_e and C_f.
p_e	$= I_R \cdot \omega L_e/V_{\text{in}}$, the normalized output current.
p_{re}	$= R/\omega L_e$, the R normalized by the reactance of L_e.
v_{Sn}	$= v_S/V_{\text{in}}$ the normalized switch voltage.
$I_{L\pi}$	Initial value of i_{in1} at $\omega t = \pi$.
$p_{\pi e}$	$= I_{L\pi} \cdot \omega L_e/V_{\text{in}}$, the normalized $I_{L\pi}$.
q	$q = 1/\omega\sqrt{L_f C_f} = \sqrt{2}q_e$, the normalized resonance frequency of L_f and C_f.
p	$= I_R \cdot \omega L_f/V_{\text{in}} = \frac{1}{2p_e}$, the normalized output current.
p_r	$= R/\omega L_f = 2p_{\text{re}}$, the R normalized by the reactance of L_f.
L_{decpl}	$= L_{\text{in}}$, resonant inductance for the uncoupled windings.
L_{cpl}	$= L_f$, resonant inductance for the coupled windings.

I. INTRODUCTION

WIRELESS power transfer (WPT) based on magnetic coupling is increasingly applied in portable devices, medical implants, electric vehicles, and so on [1]–[5]. In most common situations, increasing the frequency is conducive to reduce the size and extend the transfer distance, but it is quite challenging to design a high-efficiency inverter for the WPT up to megahertz. The efficiency deteriorates because of the substantial increase in the losses of switches and magnetic components.

A class-E inverter with a finite dc-feed inductance is often used for the WPT, in which the load varies in a wide range. The switch can naturally achieve zero-voltage switching (ZVS) without using closed-loop control, but this expected feature is essentially based on using much lower input inductance [6]–[8]. It results in a large ac current through the input inductor and the dc source. The current causes not only additional losses, but also conducted electromagnetic interference (EMI).

Manuscript received December 25, 2018; revised March 21, 2019; accepted May 3, 2019. Date of publication May 8, 2019; date of current version October 18, 2019. This work was supported in part by the National Natural Science Foundation of China under Grant 51607039, in part by the Natural Science Foundation of Fujian Province of China under Grants 2018J01623 and 2019J01772, and in part by the Program for the Training of Distinguished Young Scientists in Fujian Provincial Universities under Grant GY-Z18161. Recommended for publication by Associate Editor J.-I. Itoh. *(Corresponding author: Xiaosheng Huang.)*

X. Huang, Y. Kong, and S. Lin are with the College of Information Science and Engineering, Fujian University of Technology, Fuzhou 350118, China (e-mail: hxs@fjut.edu.cn; kongyipeng1992@qq.com; linshuyi1985@qq.com).

Z. Ouyang is with the DTU Elektro, Technical University of Denmark, 2800 Kongens Lyngby, Denmark (e-mail: zo@elektro.dtu.dk).

W. Chen is with the College of Electrical Engineering and Automation, Fuzhou University, Fuzhou 350118, China (e-mail: chw@fzu.edu.cn).

Color versions of one or more of the figures in this paper are available online at http://ieeexplore.ieee.org.

Digital Object Identifier 10.1109/TPEL.2019.2915770

Interleaving two class-E inverters is effective for suppressing the odd-order harmonics through the dc source. The combined topology is known as push–pull class-E inverter [9], [10], differential-mode class-E inverter [11]. The even-order harmonics remaining can also be reduced by coupling the input inductors of the interleaved inverters. Hence, the ripple current through the dc source can be suppressed significantly to reduce EMI noise. This approach was introduced in [12], but the design criterion to achieve ZVS was still unclear.

In the push–pull class-E inverter with a finite dc-feed inductance, the amplitude of the ac current through the input inductors is kept relatively large to maintain ZVS when the load varies. For loss reduction, a possible approach is reducing the amplitude by an adjustable input voltage, but it requires an additional dc–dc converter [13]. The other approach is reducing the equivalent series resistance (ESR) of the inductors by using a larger size of the magnetic elements. Consequently, individual inductors with air-core or low-permeability cores are usually applied in the class-E inverters. The inductor size is relatively big and difficult to be reduced.

The design methodologies of the inductors of class-E inverters are basically the same as conventional power converters. Saini *et al.* [14] propose a detailed design method of choke inductors for parallel-capacitor class-E inverters, but it cannot be used for the inductor with a large ac current. Zhang *et al.* [15] introduce a design method to reduce the volume of inductors with a significant ac current. However, by now, most of the existing literature about class-E inverters focuses on the circuit design and closed-loop control, but not the magnetic design [6], [8], [16]–[21].

Magnetic integration methods, particularly coupling multiple inductors, have been proved highly effective for improving performance and reducing the size of power converters [22]–[24]. When the two inductors of a push–pull class-E inverter are integrated, the circuit board area occupied by the inductors can be reduced directly. Moreover, the class-E inverter presents improved harmonic suppression by coupling the inductor windings. However, so far, few studies have discussed the magnetic integration of the class-E inverter.

This paper presents the circuit design and magnetic integration of push–pull class-E inverters for the WPT up to megahertz. The circuit analysis, design, and comparison of the class-E inverters with either coupled or uncoupled windings are first presented in Section II. It shows that the even-order harmonic currents through the integrated inductor are suppressed by coupling the windings. Then, a design criterion to satisfy ZVS of the push–pull class-E inverter with coupled windings is proposed. In Section III, the approaches of magnetic integration are analyzed and compared. A new magnetic structure, which consists of hybrid materials with different permeability, is proposed to reduce the number of gaps and simplify the magnetic design. The structure is implemented for the two kinds of integrated inductors with either coupled or uncoupled windings. In Section IV, a 3-MHz WPT system is built, and the topologies of the class-E inverters are also applied for rectification. A detailed comparison (regarding efficiency, harmonic current, and temperature rise) for different integrated inductors is presented.

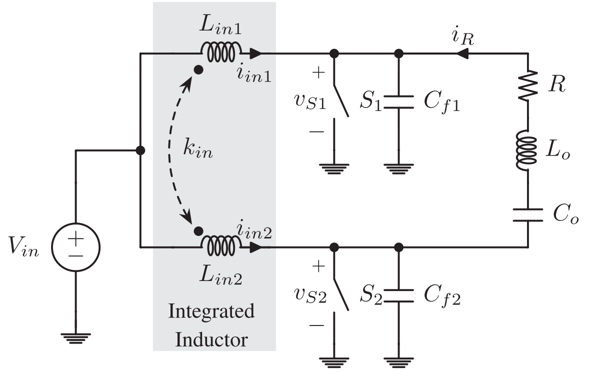

Fig. 1. Push–pull class-E inverter with an integrated inductor. The windings (L_{in1} and L_{in2}) can be either coupled or uncoupled.

II. CIRCUIT DESIGN

As shown in Fig. 1, the windings of the integrated inductor can be either coupled or uncoupled; thus, the circuit design is different for the cases. If the windings are uncoupled, i.e., $k_{\mathrm{in}} = 0$, the circuit design is the same as a single-switch class-E inverter and has been well studied in the existing literature[6], [8]. Note that the current amplitude of the inductor windings is kept large to satisfy ZVS when the load resistance varies from an optimal value to infinity. Since the switches are driven by complementary signals, the inverter operates in a differential mode. Hence, the fundamental and odd-order harmonic currents circulate in the inverter, while the even-order ones can pass through the dc source.

For the other case, i.e., $k_{\mathrm{in}} \neq 0$, the ripple current of the dc source can be suppressed by coupling the windings. This topology has been proposed in [12], but its design criteria to achieve ZVS are still unknown. Therefore, in this section, the analysis focuses on the inverter with coupled windings.

A. Switch Voltage for Coupled Windings

For the topology with coupled windings, the designed inductance for different order harmonics can be separated. The inductance for even-order harmonic currents is equal to the self-inductance of the windings. On the other hand, the inductance for fundamental and odd-order harmonic currents is equal to the leakage inductance. Therefore, higher self-inductance of the coupled windings is preferred for ripple suppression, while the leakage inductance should be kept at a particular value to satisfy ZVS. Hence, the ideal integrated inductor with coupling windings acts like a transformer with a particular leakage inductance. Since the switching behavior is changed by the coupled windings, it requires a new design criterion to achieve ZVS, as well as conventional class-E inverters. To simplify the analysis below, some assumptions are made as follows.

1) The switches have zero ON-resistance and infinite OFF-resistance. The switch S_1 is ON for $0 < \omega t \leq \pi$ and OFF for $\pi < \omega t \leq 2\pi$. In reverse, S_2 is OFF for $0 < \omega t \leq \pi$ and ON for $\pi < \omega t \leq 2\pi$. Hence, the switch voltages satisfy

$$v_s(\omega t) = v_{s1}(\omega t) = v_{s2}(\omega t + \pi). \quad (1)$$

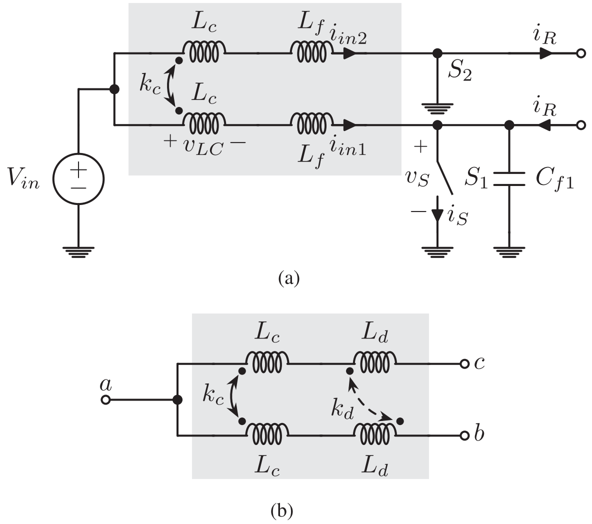

Fig. 2. Equivalent circuit when S_1 is OFF for $\pi < \omega t \leq 2\pi$. The coupling coefficient $k_c = 1$. The value of k_d depends on the magnetic structure, and $L_f = (1 + k_d)L_d$. (a) Equivalent circuit with OFF-state S_1. (b) Equivalent model of the integrated inductor with coupled windings.

2) The ESR of passive components is ignored.
3) Q_L is high enough to make the output current i_R a purely sinusoidal wave expressed as

$$i_R(\omega t) = I_R \cdot \sin(\omega t + \varphi). \tag{2}$$

The L_o and C_o resonate at the operation frequency, i.e., $\omega = 1/\sqrt{L_o C_o}$.

4) The mutual inductance and leakage inductance, i.e.,

$$L_c = k_{\text{in}} L_{\text{in}} \tag{3}$$

$$L_f = (1 - k_{\text{in}}) L_{\text{in}} \tag{4}$$

satisfy $L_c \gg L_f$. Thus, the winding current can be decomposed by a dc and an ac as

$$i_{\text{in}1}(\omega t) = I_{\text{DC}} + i_{Lf}(\omega t) \tag{5}$$

$$i_{\text{in}2}(\omega t) = I_{\text{DC}} - i_{Lf}(\omega t). \tag{6}$$

Since the circuit units are symmetrical, the winding currents satisfy

$$i_{Lf}(\omega t) = -i_{Lf}(\omega t + \pi) \tag{7}$$

which implies that there is no common-mode current if the windings are coupled and the self-inductance is large enough. The even-order harmonic currents can be eliminated theoretically.

Fig. 2(a) illustrates the equivalent circuit of the inverter when S_1 is OFF. The C_{f2} is removed from the circuit since it is shorted by the ON-state S_2. The integrated inductor is simply formed by the mutual inductance L_c and the leakage inductance L_f. Usually, the equivalent model of the inductor can also be described by two coupled parts, as shown in Fig. 2(b), for satisfying energy conservation. The latter model can be transformed by using $L_f = (1 + k_d)L_d$ for the analysis below.

The coupled windings act as a transform with a particular leakage inductance because $L_c \gg L_f$. Therefore, when S_2 is shorted for $\pi < \omega t \leq 2\pi$, the voltage across L_c is

$$v_{Lc}(\omega t) = V_{\text{in}} + \omega L_f \frac{di_{Lf}(\omega t)}{d\omega t}. \tag{8}$$

From (7) and (8), the charging current of C_{f1} for $\pi < \omega t \leq 2\pi$ satisfies

$$\omega C_f \frac{dv_S(\omega t)}{d\omega t} = \frac{-1}{\omega L_e} \int_{\pi}^{\omega t} v_S(\omega t_1)\, d\omega t_1 + I_{L\pi} + i_R(\omega t) \tag{9}$$

which can be represented by a second-order differential form expressed as

$$\frac{1}{q_e^2} \frac{d^2 v_{Sn}(\omega t)}{d\omega t^2} + v_{Sn}(\omega t) - p_e \cdot \cos(\omega t + \varphi) = 0. \tag{10}$$

The general solution of (10) is

$$v_{Sn}(\omega t) = \xi_1 \cos(q_e \omega t) + \xi_2 \sin(q_e \omega t) - \xi_e \cos(\omega t + \varphi) \tag{11}$$

where $\xi_e = q_e^2 p_e/(1 - q_e^2)$; ξ_1 and ξ_2 are the coefficients related to the circuit parameters of the inverter. Calculating the derivative of (11) gives

$$\frac{dv_{Sn}(\omega t)}{d\omega t} = \xi_2 \cos(q_e \omega t) - \xi_1 \sin(q_e \omega t) + \xi_e \sin(\omega t + \varphi). \tag{12}$$

From (9) and (12) at $\omega t = \pi$, the initial conditions can be expressed by

$$v_{Sn}(\pi) = 0 \tag{13}$$

$$\left.\frac{dv_{Sn}(\omega t)}{d\omega t}\right|_{\omega t = \pi} = q_e^2 p_{\pi e} - q_e^2 p_e \sin(\varphi). \tag{14}$$

Solving (11) based on the initial conditions results in the expressions of ξ_1 and ξ_2 given by

$$\begin{aligned} \xi_1 = &- \xi_e \left[\cos(\pi q_e)\cos(\varphi) + \frac{1}{q_e}\sin(\pi q_e)\sin(\varphi)\right] \\ &- q_e \sin(\pi q_e) \cdot [p_{\pi e} - p_e \sin(\varphi)] \\ \xi_2 = &- \xi_e \left[\sin(\pi q_e)\cos(\varphi) - \frac{1}{q_e}\cos(\pi q_e)\sin(\varphi)\right] \\ &+ q_e \cos(\pi q_e) \cdot [p_{\pi e} - p_e \sin(\varphi)]\,. \end{aligned} \tag{15}$$

To get the switch voltage for a particular value of q_e, we require three constraint expressions for calculating unknown state variables (p_e, $p_{\pi e}$, and φ). In this paper, the constraint conditions include: 1) volt–second balance of windings; 2) energy conservation; and 3) Ohm's law for the fundamental voltage and current. The equations are deduced as follows.

1) According to the volt–second balance principle, the OFF-state switch voltage v_{Sn} defined in Assumption 1) for $\pi < \omega t \leq 2\pi$ satisfies

$$2\pi = \int_{\pi}^{2\pi} v_{Sn}(\omega t_1)\, d\omega t_1. \tag{16}$$

Substituting (11) into (16) results in

$$\begin{aligned} p_{\pi e} = 2 \cdot \frac{\pi + \xi_e \sin(\varphi)}{1 - \cos(\pi q_e)} + \frac{\xi_e \cos(\varphi)\sin(\pi q_e)}{q_e(1 - \cos(\pi q_e))} \\ + \left(p_e - \frac{\xi_e}{q_e^2}\right)\sin(\varphi). \end{aligned} \tag{17}$$

2) As the input voltage is constant, the input energy g_{in} per period is

$$g_{\text{in}} = \frac{2\pi}{\omega} \cdot V_{\text{in}} I_{\text{DC}} = \frac{2\pi}{\omega} \cdot V_{\text{in}} \cdot \frac{i_{\text{in1}}(\pi) + i_{\text{in1}}(2\pi)}{2}. \quad (18)$$

From (5), (6), (7), and (12), we obtain

$$\begin{aligned} \beta_{\text{IDC}} &= \frac{2 I_{\text{DC}}}{V_{\text{in}} \omega C_f} \\ &= q_e^2 p_{\pi e} - q_e^2 p_e \sin(\varphi) + \left. \frac{d v_{Sn}(\omega t)}{d\omega t} \right|_{\omega t = 2\pi}. \end{aligned} \quad (19)$$

The energy dissipation per period g_{out} consists of the energy consumption of R and the loss of C_{f1}. It can be expressed as

$$\frac{g_{\text{out}}}{V_{\text{in}}^2 C_f} = \pi q_e^2 p_e^2 p_{\text{re}} + \frac{1}{2} v_{Sn}(2\pi)^2. \quad (20)$$

Combining (18)–(20) gives the equation for energy conservation as

$$\pi \cdot \beta_{\text{IDC}} = \pi q_e^2 p_e^2 p_{\text{re}} + \frac{1}{2} v_{Sn}(2\pi)^2. \quad (21)$$

3) According to the symmetry shown in (5)–(7), the input current i_{in} can be normalized as

$$\begin{aligned} \beta_{\text{in}}(\omega t) &= \frac{i_{\text{in1}}(\omega t)}{V_{\text{in}} \omega C_f} \\ &= \begin{cases} \beta_{\text{IDC}} - \beta_{\text{in}}(\omega t + \pi), & 0 < \omega t \leq \pi \\ \frac{d v_{Sn}(\omega t)}{d\omega t} - q_e^2 p_e \sin(\omega t + \varphi), & \pi < \omega t \leq 2\pi. \end{cases} \end{aligned} \quad (22)$$

From (9), the normalized switch current $i_S(\omega t)$ for $0 < \omega t \leq \pi$ is

$$\beta_S(\omega t) = \frac{i_S(\omega t)}{V_{\text{in}} \omega C_f} = \beta_{\text{in}}(\omega t) - q_e^2 p_e \sin(\omega t + \varphi). \quad (23)$$

At the switching-ON instant without ZVS condition, C_{f1} is discharged through S_1. According to charge conservation, the transient integral can be theoretically given by

$$\int_0^{0+} i_S(\omega t_1)\, d\omega t_1 = V_{\text{in}} \omega C_f \cdot v_{Sn}(2\pi). \quad (24)$$

The fundamental current flowing through the switch can be decomposed into two quadrature components. Since the inductance L_c only affects the common-mode currents, the third constraint condition can be written as

$$\begin{aligned} &\frac{\int_0^\pi \beta_S(\omega t_1) \cos(\omega t_1 + \varphi)\, d\omega t_1 + v_{Sn}(2\pi) \cos(\varphi)}{\int_0^\pi \beta_S(\omega t_1) \sin(\omega t_1 + \varphi)\, d\omega t_1 + v_{Sn}(2\pi) \sin(\varphi)} \\ &\quad = \frac{R}{2} \left(\omega C_f - \frac{1}{\omega L_f} \right) = \left(\frac{1}{q^2} - 1 \right) p_r. \end{aligned} \quad (25)$$

As a result, three state variables (p_e, $p_{\pi e}$, and φ) can be numerically solved out from the constraint equations with particular circuit parameters q_e and p_{re}.

B. Parameters for Satisfying ZVS and Zero-Voltage-Derivative Switching (ZVDS) Simultaneously

The optimum condition of a class-E inverter is normally defined as satisfying ZVS and ZVDS simultaneously. As the switching voltage and current are zero, the inverter can achieve minimum switching losses in practical systems. The optimum conditions can be expressed as

$$v_{Sn}(2\pi) = 0 \quad (26)$$

$$\left. \frac{d v_{Sn}(\omega t)}{d\omega t} \right|_{\omega t = 2\pi} = 0. \quad (27)$$

Solving the equation set formed by (16), (21), and (25)–(27), the optimum q and p_r for the inverter with coupled windings are

$$q_{\text{optm1}} = 1.659, \ p_{\text{roptm1}} = 1.197. \quad (28)$$

In the definitions $q = 1/\omega\sqrt{L_f C_f}$ and $p_r = R/\omega L_f$ for the inverter with coupled windings, L_f equals the inductance for the differential-mode current (i.e., fundamental and odd-order harmonic currents).

In contrast, for the inverter with uncoupled windings, the definitions should be changed to $q_{\text{trd}} = 1/\omega\sqrt{L_{\text{in}} C_f}$ and $p_{\text{rtrd}} = R/\omega L_{\text{in}}$, where the inductance for the differential-mode current is L_{in}.

The optimum q_{trd} and p_{rtrd} can be calculated as a class-E inverter with a finite dc-feed inductance. According to the calculation in [7], the optimum circuit parameters are

$$q_{\text{optm2}} = 1.412, \ p_{\text{roptm2}} = 1.364. \quad (29)$$

Note that L_{in} is limited by the design criterion of the class-E inverter with a finite dc-feed inductance. Therefore, using uncoupled windings will not directly improve the suppression of odd-order harmonic currents. Contrarily, it may reduce the suppression since q_{optm2} is slightly lower than q_{optm1}. As shown in Fig. 3, there is no distinct difference between the switch voltages for the coupled and uncoupled windings, while the winding current amplitude is observably reduced by using the coupled windings.

C. Parameters for Satisfying Only ZVS

The selection of circuit parameters can be more flexible by relaxing the switching conditions to achieving only ZVS. Table I is obtained by removing (27) from the equation set and presetting q values. The waveforms for different cases are illustrated in Fig. 4. It shows that the peak switch voltage decreases with a lower q value, but the winding current amplitude at $q = 1.45$ increases to about two times that at $q = 1.659$. In contrast, when $q > 1.8$, the amplitude tends to be unchanged.

Fig. 5 illustrates the switch voltages with different q and R. The switch satisfies ZVS when $R > R_{\text{rated}}$. Note that switching with a conductive body diode of MOSFET is regarded as ZVS. The peak switch voltage has a larger range of variation when R varies with a higher q value. On the other hand, the switch voltages at $q = 1.45$ tend to be load independent. Therefore, the value of q affects the winding currents and switch voltages significantly.

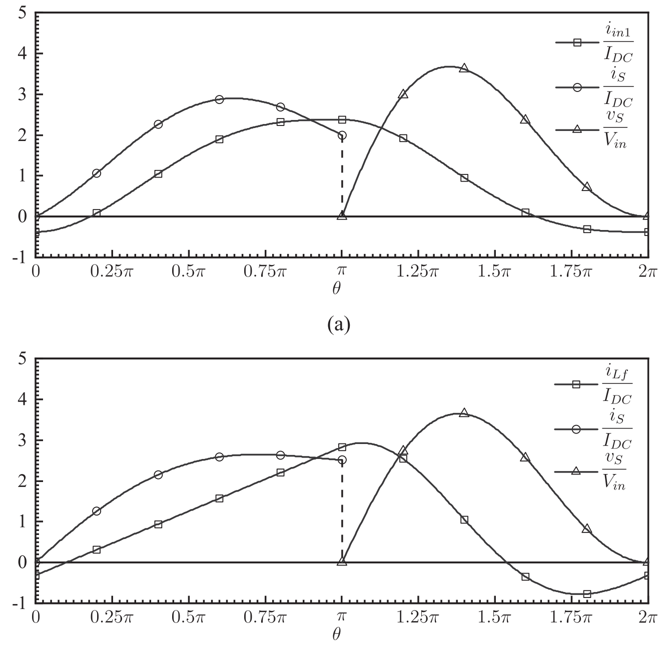

(a)

(b)

Fig. 3. Normalized waveforms of class-E inverters satisfying both ZVS and ZVDS. The peak-to-peak input current in (a) is about 25.7% lower than that in (b), and the switching-OFF current is also decreased by 20.4%. (a) Waveforms for coupled windings. (b) Waveforms for uncoupled windings.

TABLE I
PARAMETER SETS FOR SATISFYING ZVS

Cases	q	p_r	p	φ
a	1.45	2.341	0.675	0.114
b	1.5	1.624	0.983	0.179
c	1.659	1.197	1.381	0.316
d	1.8	1.151	1.491	0.415
e	1.95	1.191	1.515	0.514

For an actual inverter, the circuit parameters can be calculated by

$$R = \frac{p^2 \cdot p_r^2 \cdot V_{\text{in}}^2}{2P_{\text{out}}} \tag{30}$$

$$L_f = \frac{R}{p_r \cdot \omega} \tag{31}$$

$$C_f = \frac{1}{L_f \cdot \omega^2} \tag{32}$$

where P_{out} is the output power of the inverter and V_{in} is the dc input voltage. The designed R is based on the rated output; thus, the ZVS can be satisfied when the load resistance varies from its rated value to infinity.

III. MAGNETIC DESIGN FOR INTEGRATED INDUCTORS

Magnetic integration is commonly implemented by combining multiple inductors of a converter. The inductor windings of the inverter after integrated can be either coupled or uncoupled. These different cases result in a significant change in the circuit design. As shown in Fig. 1, the parallel capacitance C_f resonates with the self-inductance L_{in} if the windings are uncoupled. In contrast, if the windings are coupled, the C_f resonates with the leakage inductance L_f. In this paper, both two kinds of integrated inductors are built and compared. We define the resonance inductance as L_{decpl} and L_{cpl} to highlight the difference between the cases.

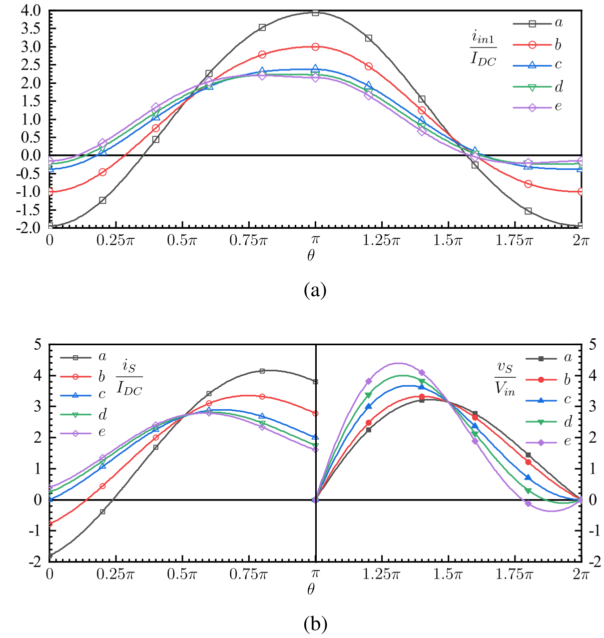

(a)

(b)

Fig. 4. Voltages and currents of the inverter with coupled windings when the value of q varies. (a) Normalized winding current. (b) Normalized switch current and voltage.

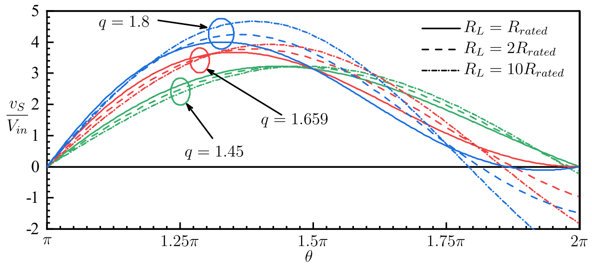

Fig. 5. Switch voltages for coupled windings with different q and load resistance.

A. Integrated Inductor With Uncoupled Windings

Designing the integrated inductor with uncoupled windings is basically the same as that for a class-E inverter with a finite dc-feed inductance. The winding inductance L_{decpl} can be expressed as

$$L_{\text{decpl}} = L_{\text{in}} = N^2 \frac{\mu_0 A_e}{l_e} \tag{33}$$

$$l_e = \frac{l_{\text{core}}}{\mu_r} + l_{\text{gap}} \tag{34}$$

where N is the number of turns, $\mu_0 = 4\pi \cdot 10^{-7}$H/m, A_e is the effective cross-sectional area of the magnetic core, l_{core} is the

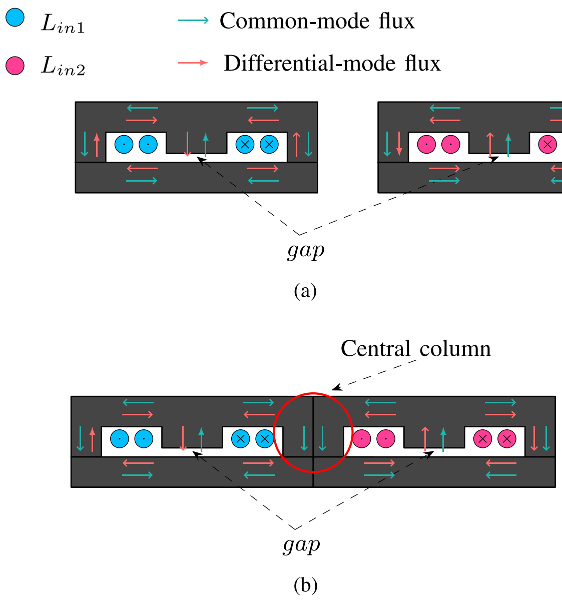

Fig. 6. Magnetic integration for uncoupled windings. The differential-mode flux through the central column is canceled by combining the individual inductors. (a) Individual inductors. (b) Integrated inductor with uncoupled windings.

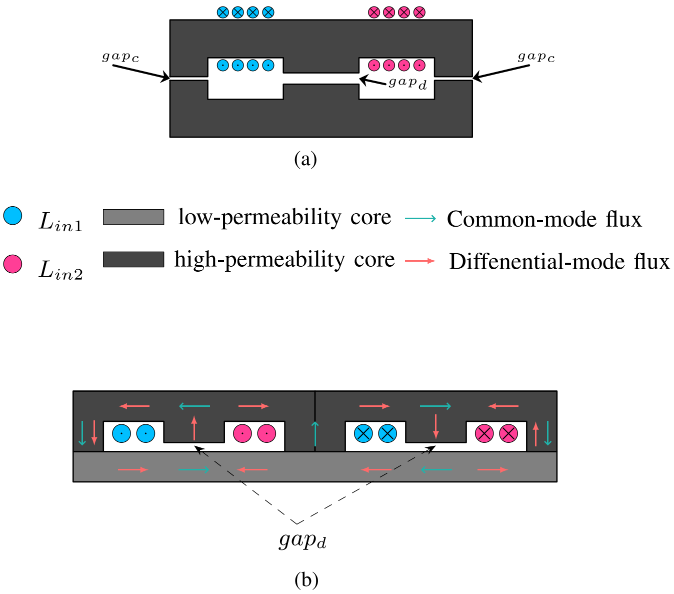

Fig. 7. Magnetic structures for the integrated inductor with coupled windings. (a) Magnetic structure with three gaps (earlier work). (b) Magnetic structure with hybrid cores (this paper).

effective magnetic path length of the core, μ_r is the relative permeability of the core, l_{gap} is the gap length, and l_e is the effective magnetic path length of L_{decpl}.

Fig. 6 illustrates the magnetic integration for the uncoupled windings. The windings share the central column after integration. The even-symmetric common-mode fluxes are unchanged in the central column. In contrast, the odd-symmetric differential-mode ones are canceled. Therefore, the core loss can be slightly reduced by suppressing the flux through the shared column.

For size reduction, the integrated method can also reduce A_e of the central column based on the same losses of individual inductors.

B. Integrated Inductor With Coupled Windings

As mentioned in Section II-A, the integrated inductor with coupled windings acts like a transformer with designed leakage inductance L_f and mutual inductance L_c. The inductance for the even-order harmonic currents is $L_f + L_c$, while the inductance for the fundamental and odd-order harmonic currents is L_f. Hence, the values of L_c and L_f can be designed separately.

Fig. 7(a) shows an "E-E"-type magnetic structure for building an integrated inductor with two coupled windings. Three gaps are set to avoid core saturation and adjust the inductance. The common-mode flux, which is excited by the dc bias [defined in (5)] and the even-order harmonic currents, flows through the gaps of side columns and bypasses the central gap. In contrast, the differential-mode flux, which is excited by the fundamental and odd-order harmonic currents, flows through all the three gaps. The suppression of even-order harmonic currents can be improved by reducing l_{gapd}, but the dc bias of the inverter may cause saturation of the magnetic cores. Therefore, the gaps should be precisely set to suppress the harmonic currents and prevent a significant increase in the inductor loss.

As illustrated in Fig. 7(b), a new magnetic structure formed by hybrid materials is proposed to reduce the number of gaps and simplify the magnetic design. The low-permeability material is introduced to avoid core saturation without using gaps on the side columns, while the high-permeability material benefits size reduction and makes sure L_c is large enough to suppress the common-mode currents. Therefore, the gap_c is removed from the new structure, and the central gap is adjusted to get a preferred L_f. The inductance for common-mode and differential-mode harmonic currents can be, respectively, expressed as

$$L_c = N^2 \frac{\mu_0 A_e}{l_{ec}} \tag{35}$$

$$l_{ec} \approx \frac{l_{\text{coreh}}}{\mu_{rh}} + \frac{l_{\text{coreh}}}{\mu_{rl}} \tag{36}$$

$$L_{\text{cpl}} = L_f = N^2 \frac{\mu_0 A_e}{l_{ef}} \tag{37}$$

$$l_{ef} = \frac{l_{\text{coreh}}}{\mu_{rh}} + \frac{l_{\text{corel}}}{\mu_{rl}} + l_{\text{gapd}} \tag{38}$$

where l_{gapc} and l_{gapd} are the length of gap_d and gap_c, respectively. l_{ef} and l_{ec} are the effective magnetic path length of L_c and L_f. l_{coreh} and l_{corel} are the effective magnetic path length of the high-permeability core and the low-permeability core, respectively. A_e is the effective cross-sectional area. Note that the defined variables are based on one "E-I"-type core.

Since $l_{ef} \gg l_{ec}$, the value of L_c is much higher than L_f. Hence, the integrated inductor with coupled windings can achieve the suppression of even-order harmonic currents without using a filter.

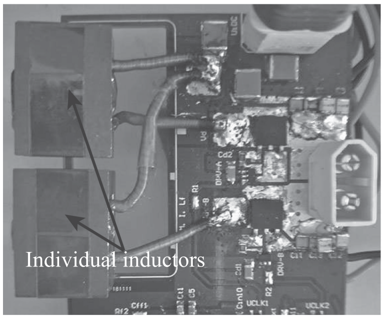

Fig. 8. Individual inductors for verifying loss reduction of the central column after magnetic integration. The output terminal is opened directly.

Besides, since the magnetic cores are arranged next to each other, the differential-mode fluxes through the central column are also canceled. However, due to the higher field density bias caused by dc bias, the total core loss is still higher than that of the integrated inductor with uncoupled windings.

C. Qualitative Analysis for Core Losses

The Steinmetz empirical equation and its improved forms are usually applied to calculate core losses of magnetic components [14], [25]–[27]. The estimated core loss P_{core} under sinusoidal flux density is given by

$$P_{\text{core}} = \gamma f^{\alpha} B_m^{\beta} \cdot V_{\text{core}} \tag{39}$$

where γ, α, and β are the coefficients extracted from the material datasheets of magnetic cores, V_{core} is the core volume, and B_m is the amplitude of excitation magnetic density. The prime part of B_m caused by the fundamental harmonic of switch voltage can be approximately calculated by

$$B_{m1} = \frac{p \cdot p_r \cdot 2V_{\text{in}}}{NA_e \cdot \omega} \tag{40}$$

where N is the number of turns of each winding and A_e is the area of the core section. According to a Fourier series of the switch voltage in Fig. 3(a), the amplitude of the second-order harmonic voltage is about 0.54 times the fundamental harmonic voltage. Hence, the flux density is nonsinusoidal; the material datasheets and the Steinmetz equation cannot be used for calculating the core losses of integrated inductors.

Due to the nonsine excitation, estimating or measuring the losses of the integrated inductor is difficult to get accurate results. A more accurate method needs to be investigated in future works. To verify the effect of magnetic integration, a more feasible method is measuring and comparing the losses for different magnetic designs. As shown in Fig. 8, two individual inductors (0.67 μH) using "E-E"-type cores (EQ25/5.6/18, PC200 material) are applied in a class-E inverter. The open-load loss is about 11.6 W (at 3 MHz). Then, the individual inductors are moved and pressed together directly when the open-load loss is being measured. The measurement is repeated continuously, and it shows that the open-load loss always instantly drops by about 0.2 W when the inductors are pressed together. There is no distinct change when measuring the system efficiency since the loss reduction is too small.

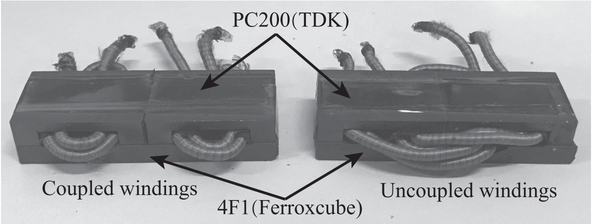

Fig. 9. Magnetic structure used for integrated inductors. For a fair comparison, we use the same cores for both kinds of integrated inductors with coupled windings and uncoupled windings.

Generally, the optimization of a gaped inductor is a multiobjective problem, which relates to winding turns, core material, fringe effect around gaps, and so on. The losses of the integrated inductor are highly dependent on a particular design. Since there is no distinct difference in system features when the individual inductors are integrated together without coupling the windings, the integrated inductor with uncoupled windings can also represent the individual inductors. In this paper, therefore, we use the proposed magnetic structure to build two kinds of integrated inductors for a fair comparison based on the same conditions. As illustrated in Fig. 9, there are two high-permeability cores (EQ25/5.6/18) of PC200 material placed on a low-permeability core (4.1-mm-thick plate) of 4F1 material. The detailed comparison is presented in the following.

IV. MEGAHERTZ WPT PROTOTYPE WITH CLASS-E INVERTERS AND RECTIFIERS

Several inverters and rectifiers with different integrated inductors are built to verify the analysis above. As illustrated in Fig. 10, the WPT system consists of three parts, i.e., the class-E inverter, the magnetic resonant tank, and the class-E rectifier. Since class-E inverters can also operate for rectification, we use the same topology for rectifiers but replace the MOSFETs by diodes. The design criteria for inverters are also applied for the rectifiers.

A. Magnetic Resonant Tank of the WPT System

The magnetic resonant tank consists of three resonant loops of which parameters meet

$$\frac{1}{\omega^2} = L_1 C_1 = L_2 C_{2\text{eq}} = L_3 C_3. \tag{41}$$

where $C_{2\text{eq}} = C_1 C_2 / (C_1 + C_2)$. The first resonant loop acts as an output filter of the class-E inverter, and the third loop acts as an input filter of the class-E rectifier. Therefore, the topology is well simplified. For a better comparison, we use the same parameters for the inverter and the rectifier. Since they are symmetrical, the voltage gain and the load resistance of the system can be approximately given by

$$\frac{V_{\text{out}}}{V_{\text{in}}} \approx \frac{k_{23}\sqrt{L_3}}{k_{12}\sqrt{L_1}} \tag{42}$$

$$R_L = \frac{V_{\text{out}}^2}{P_{\text{out}}} \tag{43}$$

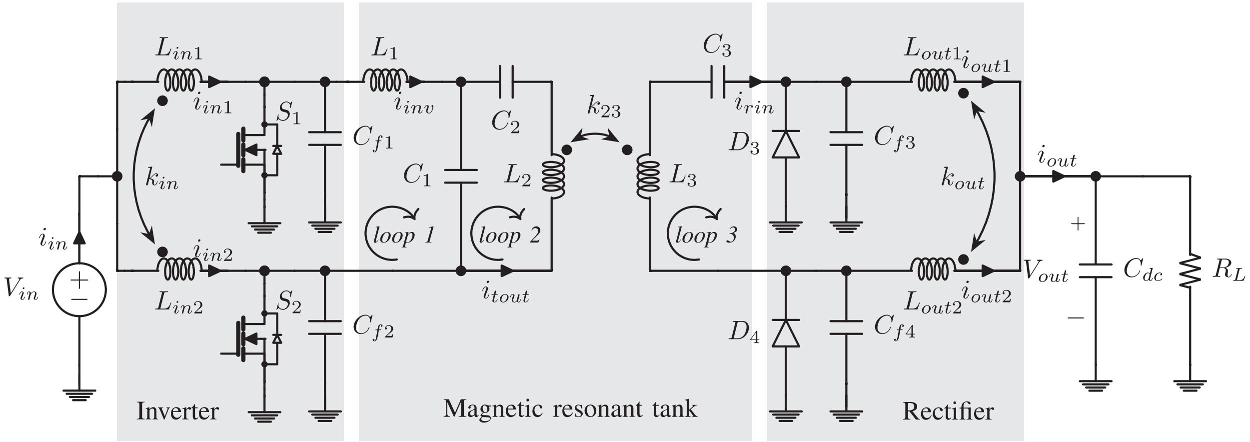

Fig. 10. Topology of the WPT prototype. The class-E rectifier has the similar topology, as well as the inverter, but it uses diodes as switching devices. When the inverter/rectifier consists of the integrated with uncoupled windings, the coupling coefficient $k_{\text{in}} = 0$.

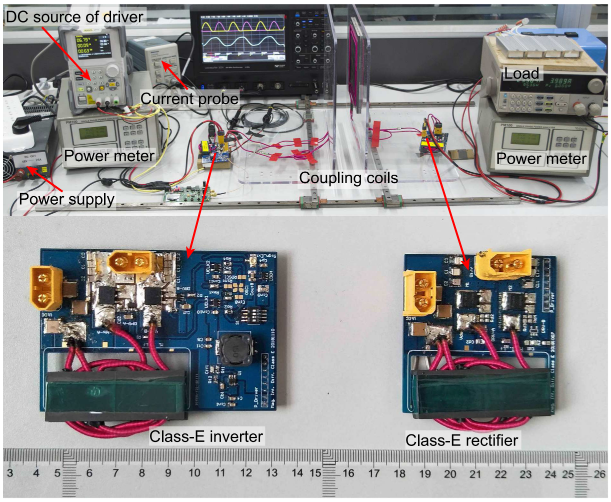

Fig. 11. Experiment setup of the WPT system. The coupling coils consist of two square coils, which are 15 cm × 15 cm. The transfer distance is fixed at 4 cm, which makes the coupling coefficient about 0.3. The inductor L_1 formed by an 8-shaped coil is integrated at the transmitting coil.

where k_{23} are the coupling coefficient between L_2 and L_3. $k_{12} = \sqrt{L_1/(L_1 + L_2)}$ is defined as the equivalent coupling coefficient. As shown in Fig. 11, the WPT system is designed to achieve a dc–dc converter (48 to 48 V) with the rated output power of about 300 W. The value of k_{23}, which is about 0.3 in this paper, is limited by the transfer distance and the coil diameters. Hence, the values of L_1, L_2, and L_3 are adjusted to realize the expected voltage gain, as shown in Table II.

B. *Experiment Setup for Inverters and Rectifiers*

1) Circuit Design and Component Selection: The parameters of the class-E inverter and rectifier with uncoupled windings are calculated based on the optimal q_{trd} and p_{rtrd}, as in (29). The circuit design is the same as a class-E inverter with a finite dc-feed inductance [7].

The circuit parameters of inverters and rectifiers with coupled windings are calculated by (30)–(32). The variables in these equations are obtained by solving the equation set discussed in Section II-C.

Note that the parameters are calculated based on the rated power of 360 W and realize an actual output power of about 300 W of the receiver considering the system losses. The operation frequency is 3 MHz according to the optimal frequency range described in material datasheets. The applied values of C_f are lower than the calculated values due to the nonlinear parasitic capacitance of switches (about 130 pF for MOSFETs, 30 pF for diodes).

Since the switching frequency is up to megahertz, the selection of switch components is critical for the system efficiency. To reduce rectification losses, the forward voltage and junction capacitance of the diodes should be as low as possible. In this paper, ultrafast diodes (FFD10UP20S) are applied for class-E rectifiers.

For class-E inverters, since the duty cycle is fixed at 50%, the requirement for rise and fall times of switches is relaxed compared to pulsewidth modulation mode converters, in which duty cycle can substantially shift from 50%. The selection of switches of class-E inverters is related to various specifications, such as the gate charge, ON-resistance, withstand voltage, rise time, and fall time. The driving losses and frequency are limited by the gate charge. The power dissipation of the MOSFET package is highly dependent on the ON-resistance, rise time, and fall time. In addition, the parallel capacitor of class-E inverters should consider the nonlinear drain–source capacitance C_{DS} of the MOSFET. Thus, the highest switching frequency of a class-E inverter is essentially limited by the value of C_{DS}. In this paper, the IXFY36N20X3 MOSFET, which has a relatively low parasitic capacitance and switching time, is selected for the class-E inverters operating at 3 MHz.

2) Integrated Inductors: The integrated inductors, which were built in Section III-C, are applied in the prototype. For a class-E inverter with coupled windings, the resonance

TABLE II
PARAMETERS OF THE WPT PROTOTYPE

Magnetic resonant tank			Coupled windings					Uncoupled windings	
			$P_{rated} = 360W$,$V_{in} = 48V$	$q = 1.659$		$q = 1.53$		$q = 1.412$	
	Calc.	Meas.[a]		Calc.	Meas.	Calc.	Meas.	Calc.	Meas.
$L_1(\mu\text{H})$	2.364	2.809	$L_{cpl}, L_{decpl}(\mu\text{H})$ of inverter	0.775	0.78	0.600	0.59	0.679	0.65, 0.68
C_1(nF)	1.191	1.002	$L_{cpl}, L_{decpl}(\mu\text{H})$ of rectifier		0.74		0.60		0.64, 0.66
$L_2(\mu\text{H})$	9.310	10.544	$R_{rated}(\Omega)$	17.48	–	16.50	–	17.45	–
C_{2eq}(nF)	0.302	0.270	C_{f1}, C_{f2}(nF)	1.319	1.200	2.002	1.860	2.079	1.940
$L_3(\mu\text{H})$	7.659	8.646	C_{f3}, C_{f4}(nF)		1.300		2.000		2.047
C_3(nF)	0.367	0.326	Switches	IXFY36N20X3 (S_1,S_2), FFD10UP20S(D_3,D_4)					

[a] Extracted from measured data of the resonant loops by an impedance analyzer (WK6500B). [b] The values of applied C_f in the table are given by the nominal values of capacitors applied on the printed circuit board.

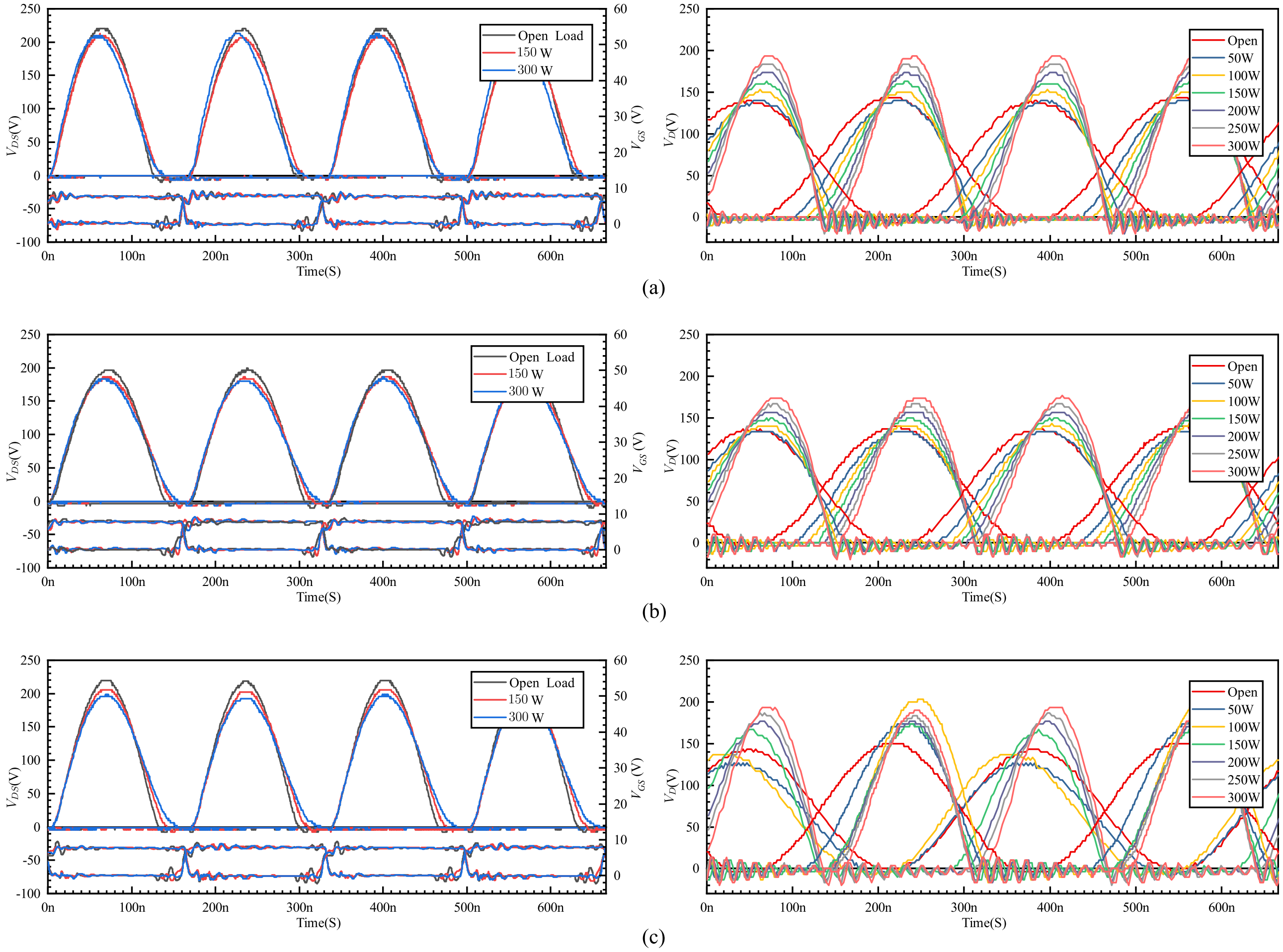

(a)

(b)

(c)

Fig. 12. Measured voltages of inverters and rectifiers. Left: drain–source voltages of MOSFETs of inverters. Right: reverse voltages of diodes of rectifiers. (a) $q = 1.659$, coupled windings. (b) $q = 1.53$, coupled windings. (c) $q = 1.412$, uncoupled windings.

inductance L_{cpl} is half of the measured value between terminals b and c of the integrated inductor illustrated in Fig. 2(b).

Likewise, for a class-E inverter with uncoupled windings, the resonance inductance L_{decpl} can be measured directly. Hence, there are two values of L_{cpl} or four values of L_{decpl} for each group of one inverter and one rectifier, as shown in Table II.

Besides, an optimized integrated inductor with coupled windings is also implemented for the comparison of magnetic losses with different core sizes. The inductance of the optimized inductor is kept the same as that with $q = 1.659$ in Table II, while the high-permeability cores (PC200, EQ25/5.6/18) are replaced by four pieces of smaller cores (PC200, ER23/5/13). The A_e is increased from 93.51 mm^2 × 2 to 50.3 mm^2 × 4, i.e., by 7.6%.

C. Measurement

1) Switch Voltage: Fig. 12 illustrates the measured voltages over the output power range from 0 to 300 W. At the output

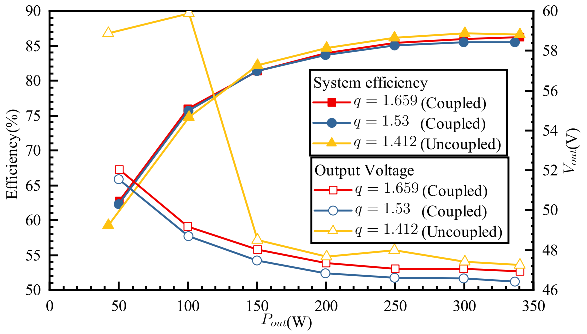

Fig. 13. Measured efficiency and output voltage with varying output power.

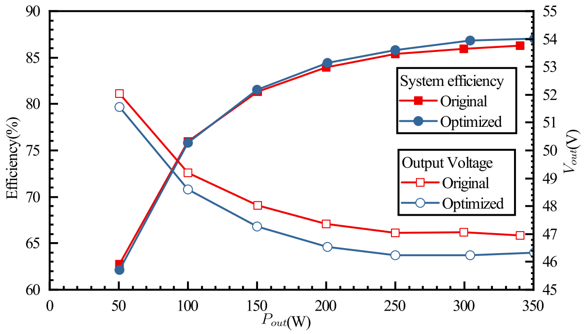

Fig. 14. Efficiency and output voltage of the prototype with the optimized integrated inductor ($q = 1.659$).

power of 300 W, the input power of inverters is about 350 W, which is close to the rated value. Due to the nonlinear parasitic capacitance of MOSFETs and diodes, the measured peak voltages are higher than the above theoretical values.

As shown in the left subfigures in Fig. 12, the ZVS is maintained over the entire load range without using closed-loop control. Comparing Fig. 12(a) and (c), when the values of q equal the optimum ones in (28) and (29), the voltage waveforms are similar despite whether the windings are coupled or uncoupled. In contrast, the voltage waveforms have lower peak values when $q = 1.53$. Therefore, a lower value of q helps reduce the required maximum $V_{\rm DS}$ of the MOSFETs selected.

For the rectifiers, according to the basic circuit analysis of the magnetic resonant tank, the input and output currents, i.e., $i_{\rm inv}$ and $i_{\rm rin}$, have the same initial phase φ_r. When the system operates at the rated load, the phase of $i_{\rm rin}$ shifted from the switching phase of D_3 meets $\varphi_r = \varphi_3 + \pi - \varphi$ for rectification. Thus, the switching phases of the class-E rectifiers satisfy

$$\varphi_3 = 2\varphi, \varphi_4 = \pi + 2\varphi \tag{44}$$

where φ_3 and φ_4 are the initial switching phases of D_3 and D_4 shifted from the driving phase of S_1. The waveforms of rectifiers and inverters are supposed to be symmetrical when MOSFETs are applied for rectification. However, since the diodes are used for the rectifiers in the prototype, the duty cycle is changed adaptively when the load varies.

As shown in Fig. 12(c), due to the slight difference in the inductance of the uncoupled windings, the diode voltages show large unbalance at 50 and 100 W. The unbalance in the voltages results in an efficiency drop. In contrast, as shown in Fig. 12(a) and (b), the diode voltages are balanced over the entire load range. Therefore, the issue of unbalanced voltages no longer exists when the windings are coupled.

The experiment results show that the class-E rectifiers present similar voltage waveforms, no matter the windings are coupled or uncoupled. However, it is worth noting that the analytic models of the class-E rectifier with coupled windings are still unclear because the analysis of the inverter cannot be applied for the rectifier when both of diodes are in OFF-state.

2) Efficiency and Output Voltage: Fig. 13 shows the system efficiency and output voltage over the output power range. The driving losses (about 0.7 W) are not considered. The output voltage of the rectifier with uncoupled windings varies shapely when lightly loaded, while that with coupled windings are more stable. The peak efficiency of the system with uncoupled windings (86.8% at 300 W) is slightly higher than that with coupled windings (86.3% at 340 W) by about 0.5%. When the output power is higher than 300 W, the ZVS tends to be lost, and the efficiency will decrease, eventually. As shown in Fig. 14, the reduced efficiency can be made up by enlarging the volume of the cores of the integrated inductor with coupled windings. Considering that the existing magnetic cores are not optimized for the integrated inductor with coupled windings, there are chances to improve the efficiency in future works further.

Fig. 15 illustrates the steady-state thermal images of the circuit boards. Cooling fans are applied but without heat sink. The inverters and rectifiers have similar thermal characteristics. The temperature rise of the integrated inductor with coupled windings is apparently higher than that with uncoupled windings. In contrast, the diode temperature of the rectifiers with coupled windings is lower. As a result, coupling the windings will increase the core losses, while decreasing the switch losses at the same conditions.

When the operation frequency is up to megahertz, a small difference in the time delay between the current probe and the voltage probe will result in a nonignorable phase shift; thus, the integral of instantaneous power will be inaccurate. Consequently, measuring the inverter/rectifier efficiency or breaking down the total losses of the circuit broad is quite difficult.

To estimate the efficiency of the class-E inverters and rectifiers, we assume that the inversion and rectification have the same efficiency, i.e., $\eta_{\rm inv} = \eta_{\rm rec}$, because they use the similar topology, integrated inductor, and component package, except the switch types (MOSFETs for inverters and diodes for rectifiers). The thermal images also show that the inverters and rectifiers have similar temperature rise at 300 W. In addition, the ESRs of the resonant loops of the magnetic resonant tank are almost constant, since the core losses of the coupling coils are negligible. The total loss of the magnetic resonant tank can be calculated according to the measured loop currents and ESRs (at 3 MHz).

The total loss of the magnetic resonant tank $P_{\rm mag}$ can be expressed by

$$P_{\rm mag} = P_{\rm in} \cdot \eta_{\rm inv} - P_{\rm out}/\eta_{\rm rec} \tag{45}$$

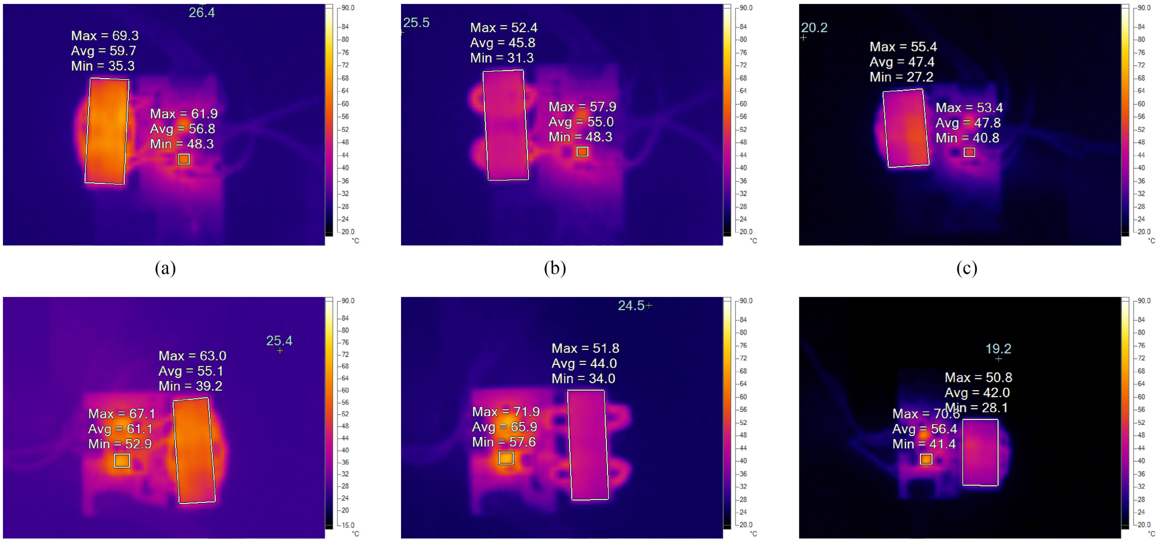

(a) (b) (c)

(d) (e) (f)

Fig. 15. Thermal steady-state image of the circuit broad of inverters and rectifiers at the 300-W output. The system efficiency at 300 W is 85.97% for coupled windings and 86.80% for uncoupled windings. By enlarging the core size of the integrated inductor with coupled windings, the system efficiency reaches 87.1% at the 350-W output. The average temperature rise of magnetic cores is reduced by about 6 °C. (a) Inverter with coupled windings. (b) Inverter with uncoupled windings. (c) Optimized inverter with coupled windings. (d) Rectifier with coupled windings. (e) Rectifier with uncoupled windings. (f) Optimized rectifier with coupled windings.

TABLE III
ESTIMATED EFFICIENCY OF CLASS-E INVERTERS AND RECTIFIERS

	P_{in}	P_{out}	$P_{loop1}(406.87\text{m}\Omega)$	$P_{loop2}(1.032\Omega)$	$P_{loop3}(553.79\text{m}\Omega)$	η_{inv}, η_{rec}
Coupled windings ($q = 1.659$)	348.6 W	299.7 W	3.42 W	4.81 W	4.27 W	94.5%
Uncoupled windings ($q = 1.412$)	346.3 W	300.6 W	3.72 W	4.73 W	4.65 W	95.1%
Coupled windings (optimized) ($q = 1.659$)	402.6 W	350.6 W	4.62 W	4.85 W	5.49 W	95.2%

where P_{in} and P_{out} are the input and output powers of the WPT system, respectively. η_{inv} and η_{rec} are the efficiencies of the inverter and the rectifier respectively.

Table III shows the estimated losses of the resonant loops and the efficiency of the class-E inverter/rectifier at the output power of 300 W. Assuming $\eta_{\text{inv}} = \eta_{\text{rec}}$ results in

$$\eta_{\text{inv}} = \eta_{\text{rec}} = \frac{P_{\text{mag}} + \sqrt{P_{\text{mag}}^2 + 4P_{\text{in}}P_{\text{out}}}}{2P_{\text{in}}} \tag{46}$$

$$P_{\text{mag}} = P_{\text{loop1}} + P_{\text{loop2}} + P_{\text{loop3}} \tag{47}$$

where P_{loop} is the loss of the resonant loop of the magnetic resonant tank. It shows that the efficiency of the inverter/rectifier with uncoupled windings is increased by about 0.6% for the same magnetic cores, while the estimated η_{inv} and η_{rec} increase to 95.2% for the optimized inductor with coupled windings.

3) Harmonic Currents: Fig. 16 shows the measured winding currents, i.e., i_{in1}. By coupling the windings of the integrated inductor, the winding current amplitudes are much lower. As shown in Fig. 16(b), the amplitude of the second-order harmonic current is distinctly reduced from 1.89 to 0.58 A at 300 W. Fig. 17 shows the fast Fourier transform (FFT) results of the input currents, i.e., i_{in}. It shows that the second-order harmonic (6 MHz) of the input current is also far lower than before. In this example,

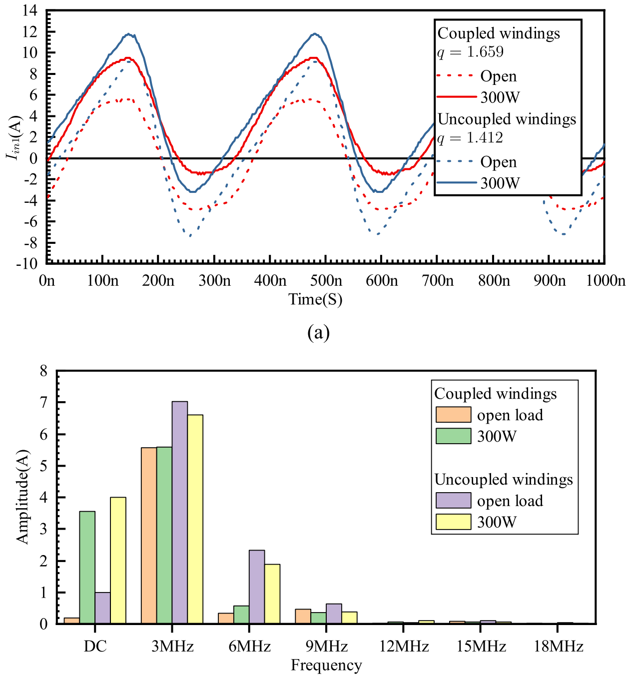

(a)

(b)

Fig. 16. Measured winding currents (i_{in1}). (a) Measured i_{in1}. (b) FFT results for i_{in1}.

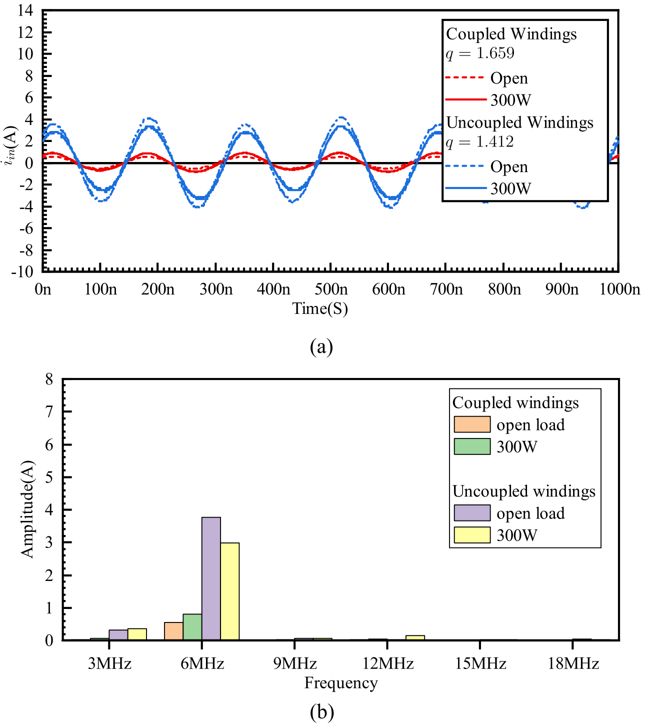

(a)

(b)

Fig. 17. Measured ripples of input currents (i_{in}). (a) Measured i_{in} (ac components). (b) FFT results for i_{in}.

the amplitude (0.8 A) is about 27% of that (2.99 A) with uncoupled windings. In addition, when the windings are uncoupled, the fundamental harmonic ripple is not canceled completely due to the slight difference in the winding inductance. Note that the measured results, which are not illustrated, for the rectifiers are similar to that of the inverters.

Therefore, although the efficiency is not improved by coupling the windings of the integrated inductors, it can naturally balance the winding currents of the class-E inverters and rectifiers and significantly suppress the harmonic currents without using EMI filters.

V. CONCLUSION

This paper focuses on the circuit design and magnetic integration of push–pull class-E inverters for the WPT up to megahertz. The design criterion is proposed to achieve ZVS of class-E inverters with coupled windings. In addition, the approach of magnetic integration is implemented. The new magnetic structure with hybrid magnetic materials is proposed to build the integrated inductors of the class-E inverters with either coupled windings or uncoupled windings. The following conclusions can be made.

1) By using the proposed design criterion, the class-E inverters with coupled windings maintain ZVS when the load resistance varies from the rated value to infinity without using any closed-loop control.
2) The integrated inductor with uncoupled windings can reduce the core loss slightly. In contrast, the integrated inductors with coupled windings can suppress the harmonic currents without using filters. In the experiment, the amplitude of the second-order harmonic current through the dc source is reduced to 27%.
3) The core losses of the class-E inverter with coupled windings are higher than that with uncoupled windings. In the experiment, the system efficiency decreases by 0.5%.
4) The winding currents of the rectifier with coupled windings are self-balanced; thus, it provides a more stable output voltage.
5) The proposed magnetic structure with hybrid materials reduces the number of the gaps of the integrated inductor and simplifies the magnetic design of class-E inverters with coupled windings.

REFERENCES

[1] Z. Zhang, H. Pang, A. Georgiadis, and C. Cecati, “Wireless power transfer—An overview,” *IEEE Trans. Power Electron.*, vol. 66, no. 2, pp. 1044–1058, Feb. 2019.

[2] C. Zhang, D. Lin, and S. Y. R. Hui, “Ball-joint wireless power transfer systems,” *IEEE Trans. Power Electron.*, vol. 33, no. 1, pp. 65–72, Jan. 2018.

[3] Y. J. Park *et al.*, “A triple-mode wireless power-receiving unit with 85.5% system efficiency for A4WP, WPC, and PMA applications,” *IEEE Trans. Power Electron.*, vol. 33, no. 4, pp. 3141–3156, Apr. 2018.

[4] T. Kan, R. Mai, P. P. Mercier, and C. C. Mi, “Design and analysis of a three-phase wireless charging system for lightweight autonomous underwater vehicles,” *IEEE Trans. Power Electron.*, vol. 33, no. 8, pp. 6622–6632, Aug. 2018.

[5] C. Xiao, D. Cheng, and K. Wei, “An LCC-C compensated wireless charging system for implantable cardiac pacemakers: Theory, experiment, and safety evaluation,” *IEEE Trans. Power Electron.*, vol. 33, no. 6, pp. 4894–4905, Jun. 2018.

[6] S. Aldhaher, D. C. Yates, and P. D. Mitcheson, “Load-independent class E/EF inverters and rectifiers for MHz-switching applications,” *IEEE Trans. Power Electron.*, vol. 33, no. 10, pp. 8270–8287, Oct. 2018.

[7] A. Grebennikov, “Switched-mode RF and microwave parallel-circuit class E power amplifiers,” *Int. J. RF Microw. Comput.-Aided Eng.*, vol. 14, no. 1, pp. 21–35, 2004.

[8] L. Roslaniec, A. S. Jurkov, A. A. Bastami, and D. J. Perreault, “Design of single-switch inverters for variable resistance/load modulation operation,” *IEEE Trans. Power Electron.*, vol. 30, no. 6, pp. 3200–3214, Jun. 2015.

[9] H. Mousavian, S. Abnavi, A. Bakhshai, and P. Jain, “A push-pull class E converter with improved PDM control,” in *Proc. IEEE 7th Int. Symp. Power Electron. Distrib. Gener. Syst.*, Jun. 2016, pp. 1–6.

[10] Z. Kaczmarczyk and W. Jurczak, “A push–pull class-E inverter with improved efficiency,” *IEEE Trans. Ind. Electron.*, vol. 55, no. 4, pp. 1871–1874, Apr. 2008.

[11] M. de Rooij and Y. Zhang, “Comparison of 6.78 MHz amplifier topologies for 33 W, highly resonant wireless power transfer,” in *Proc. Int. Exhib. Conf. Power Electron., Intell. Motion, Renew. Energy Energy Manage.*, Jun. 2017, pp. 1–7.

[12] H. Xiaosheng and C. Wei, “WPT topology scheme with dual parallel-circuit class E inverters and integrated inductor,” in *Proc. IEEE Int. Electron. Appl. Conf. Expo.*, Nov. 2014, pp. 635–638.

[13] M. Fu, H. Yin, M. Liu, Y. Wang, and C. Ma, “A 6.78 MHz multiple-receiver wireless power transfer system with constant output voltage and optimum efficiency,” *IEEE Trans. Power Electron.*, vol. 33, no. 6, pp. 5330–5340, Jun. 2018.

[14] D. K. Saini, A. Ayachit, A. Reatti, and M. K. Kazimierczuk, “Analysis and design of choke inductors for switched-mode power inverters,” *IEEE Trans. Power Electron.*, vol. 65, no. 3, pp. 2234–2244, Mar. 2018.

[15] Z. Zhang, K. D. T. Ngo, and J. L. Nilles, “Design of inductors with significant ac flux,” *IEEE Trans. Power Electron.*, vol. 32, no. 1, pp. 529–539, Jan. 2017.

[16] M. Liu, M. Fu, and C. Ma, “Parameter design for a 6.78-MHz wireless power transfer system based on analytical derivation of class E current-driven rectifier,” *IEEE Trans. Power Electron.*, vol. 31, no. 6, pp. 4280–4291, Jun. 2016.

[17] S. Park and J. Rivas-Davila, “Duty cycle and frequency modulations in class-E dc–dc converters for a wide range of input and output voltages,” *IEEE Trans. Power Electron.*, vol. 33, no. 12, pp. 10524–10538, Dec. 2018.

[18] M. Liu, Y. Qiao, S. Liu, and C. Ma, “Analysis and design of a robust class e^2 dc-dc converter for megahertz wireless power transfer,” *IEEE Trans. Power Electron.*, vol. 32, no. 4, pp. 2835–2845, Apr. 2017.

[19] S. Liu, M. Liu, S. Yang, C. Ma, and X. Zhu, “A novel design methodology for high-efficiency current-mode and voltage-mode class-e power amplifiers in wireless power transfer systems,” *IEEE Trans. Power Electron.*, vol. 32, no. 6, pp. 4514–4523, Jun. 2017.

[20] S. Liu, M. Liu, S. Han, X. Zhu, and C. Ma, “Tunable class e^2 dc-dc converter with high efficiency and stable output power for 6.78-MHz wireless power transfer,” *IEEE Trans. Power Electron.*, vol. 33, no. 8, pp. 6877–6886, Aug. 2018.

[21] S. Aldhaher, P. C. K. Luk, and J. F. Whidborne, “Tuning class E inverters applied in inductive links using saturable reactors,” *IEEE Trans. Power Electron.*, vol. 29, no. 6, pp. 2969–2978, Jun. 2014.

[22] M. H. Ahmed, C. Fei, F. C. Lee, and Q. Li, “48-V voltage regulator module with PCB winding matrix transformer for future data centers,” *IEEE Trans. Ind. Electron.*, vol. 64, no. 12, pp. 9302–9310, Dec. 2017.

[23] C. Fei, Y. Yang, Q. Li, and F. C. Lee, “Shielding technique for planar matrix transformers to suppress common-mode EMI noise and improve efficiency,” *IEEE Trans. Ind. Electron.*, vol. 65, no. 2, pp. 1263–1272, Feb. 2018.

[24] A. A. Khan, H. Cha, and H. Kim, “Magnetic integration of discrete-coupled inductors in single-phase direct PWM ac-ac converters,” *IEEE Trans. Power Electron.*, vol. 31, no. 3, pp. 2129–2138, Mar. 2016.

[25] A. Ayachit and M. K. Kazimierczuk, “Steinmetz equation for gapped magnetic cores,” *IEEE Magn. Lett.*, vol. 7, 2016, Art. no. 1302704.

[26] J. Muhlethaler, J. Biela, J. W. Kolar, and A. Ecklebe, “Core losses under the dc bias condition based on Steinmetz parameters,” *IEEE Trans. Power Electron.*, vol. 27, no. 2, pp. 953–963, Feb. 2012.

[27] C. P. Steinmetz, “On the law of hysteresis,” *Proc. IEEE*, vol. 72, no. 2, pp. 197–221, Feb. 1984.

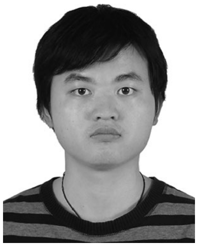

Xiaosheng Huang received the B.E. and Ph.D. degrees from Fuzhou University, Fuzhou, China, in 2009 and 2015, respectively.

He is currently an Associate Professor with the College of Information Science and Engineering, Fujian University of Technology, Fuzhou. He is also with the Fujian Provincial University Engineering Research Center for Industrial Automation, Fujian University of Technology. His current research interests include power conversion, high-frequency magnetics, wireless power transfer, and electromagnetic field analysis and applications.

Dr. Huang is a member of the Magnetic Component Specialty Committee of the China Power Supply Society.

Yipeng Kong received the B.E. degree from Suzhou University, Anhui, China, in 2016. He is currently working toward the M.E. degree in electrical engineering with the College of Information Science and Engineering, Fujian University of Technology, Fuzhou, China.

His research interests include high-frequency magnetics and wireless power transfer.

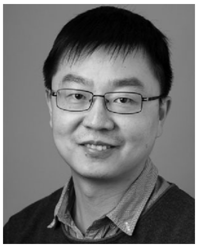

Ziwei Ouyang (S’07–M’11–SM’17) received the Ph.D. degree from the Technical University of Denmark (DTU), Kongens Lyngby, Denmark, in 2011.

Since April 2016, he has been an Associate Professor with DTU, where he was a Postdoctoral Researcher from 2011 to 2013 and an Assistant Professor from 2013 to 2016. He has more than 70 high-impact IEEE journals and conference publications and is a co-author of a chapter on Magnetics in the book entitled *Power Electronics Handbook* (Oxford, U.K.: Butterworth-Heinemann, 2018). He holds eight international patents. His research interests include high-frequency planar magnetics modeling and integration, high-density high-efficiency power converters, photovoltaic battery energy storage systems, and wireless charging.

Dr. Ouyang was a recipient of the Young Engineer Award at PCIM Asia 2014 and the Best Ph.D. Dissertation of the Year Award 2012 from the Technical University of Denmark. He received several Best Paper awards in IEEE sponsored international conferences. He has been invited to give lectures in many universities, enterprises, and educational, seminars and workshops around the world including the USA, Europe, and China. He has served as a Session Chair in some IEEE sponsored conferences and an Associate Editor for the IEEE JOURNAL OF EMERGING AND SELECTED TOPICS IN POWER ELECTRONICS.

Wei Chen received the M.S. and Ph.D. degrees from Fuzhou University, Fuzhou, China, in 1987 and 1990, respectively.

He was a Senior Visiting Professor with the Center for Power Electronics Systems, Virginia Tech, Blacksburg, VA, USA, from 1996 to 1998. He was with Delta Electronics Co. Ltd. as an R&D Manager with the Delta Power Electronics Center, Shanghai, China, from 1999 to 2008. He is currently a Professor with the College of Electrical Engineering and Automation, Fuzhou University. He has authored or coauthored more than 80 technical papers including IEEE Transactions and Proceedings. He has held more than 40 approved patents in both China and the USA. His current research interests include power conversion, high-frequency magnetics, electromagnetic interference debugging and solutions, wireless power transfer, and electromagnetic field analysis and applications.

Dr. Chen is an Executive Member of the Council of the China Power Supply Society (CPSS). He served as the Chairman of the Magnetic Component Specialty Committee of the CPSS.

Shuyi Lin received the B.E. and Ph.D. degrees from Fuzhou University, Fuzhou, China, in 2008 and 2014, respectively.

She is currently an Associate Professor with the College of Information Science and Engineering, Fujian University of Technology, Fuzhou. She is also with the Fujian Provincial University Engineering Research Center for Industrial Automation, Fujian University of Technology. Her current research interests include power conversion, high-frequency magnetics, and wireless power transfer.